# Millimeter Wave Photonic Tightly Coupled Array

Victoria A. Carey, Matthew R. Konkol, Shouyuan Shi, Andrew J. Mercante, Kevin Shreve, Andrew A. Wright, Christopher A. Schuetz, and Dennis W. Prather, *Fellow, IEEE*

***Abstract*— We present a tightly coupled array antenna excited by high-power photodiodes for millimeter wave transmit operation. The design includes thinned photodiode substrates for improved bandwidth performance at high frequency combined with the inherently lightweight, low-loss, and direct feeding architecture afforded by the photonic approach. Circuit and full wave simulations are conducted for array design and compared against the traditional electronic arrays in the literature. A prototype 1 × 3 photonic array is developed and characterized to validate the design which achieves a 3 dB (VSWR < 1.4) radiated power bandwidth of 4.6:1 across 13–60 GHz and maintains a 3 dB bandwidth near 4:1 across scan angles up to 30°. The fabricated array exhibits a 3 dB radiated power bandwidth of 1.8:1 across 30–55 GHz and a maximum measured effective isotropic radiated power of 19.4 dBm at 40 GHz.**

***Index Terms*— High-power photodiode, optically fed phased array, RF photonics, tightly coupled array (TCA) antenna, ultrawideband (UWB).**

## I. Introduction

PHASED array antennas are essential in the development of advanced multifunctional RF systems that serve both commercial and defense sectors. Emphasis in the defense community is placed on the consolidation of RF front ends, signal processing algorithms, and control centers with adaptive subsystems effective for radar and communication [1], [2]. Consolidation of RF front ends with adaptive, multifunctional capabilities requires phased arrays with multioctave operational bandwidths, high transmit power and beam space diversity, frequency agility, scaling potential, and optimal size, weight, and power (SWaP). Similar requirements are of interest in the commercial sector where these benefits can be leveraged in the fifth-generation (5G) cellular communications and mobile networks [3]. Generally, 5G encapsulates the modern trend to continually increase wireless data capacity. Specifically, increasing data capacity ultimately requires increased signal-to-noise ratio and bandwidth. To address bandwidth, signal carriers are shifting toward millimeter wave (mmW) frequencies (30–300 GHz) where increased bandwidths are attainable. For these mmW carriers, high-power phased arrays are the preferred transmit aperture as highly directional beams can compensate for increased free-space path loss [4] and atmospheric losses [5] and enable spatial-spectral channels for frequency reuse [6]. In addition to the highly directional beams, multioctave operation can enable access to allocated mmW spectrum at 24, 28, 37, 39, and 47 GHz [7] simultaneously, i.e., with a single RF front end. Much like the requirements for defense architectures, these emerging 5G mmW networks that employ dense picocell topologies demand an emphasis on scaling potential and optimal SWaP in addition to ultrawide bandwidth.

Bandwidth continues to motivate the antenna community as creative practical implementations seek to approach theoretical ideals. Radiating elements such as spirals, tapered slots, and bowties have theoretically infinite bandwidths [8], with their finite counterparts exhibiting bandwidths as high as 10:1 [9], 12:1 [10], and 21:1 [11], respectively, when tightly coupled. This mutual, or *tight*, coupling between elemental radiators is a design technique employed to extend the low-frequency bandwidth of a, theoretically, frequency-independent current sheet array (CSA) [12]. The CSA excites a uniform current distribution that radiates bilaterally at broadside and exhibits frequency-independent scanning performance [12], [13]. In principle, this frequency independence is ideal and is closely approximated by a connected array (CA): an electrically large 2-D array of electrically small connected dipoles [15]–[17]. In practice, CAs are the closest approximation to the CSA, but their bilateral radiation is often undesirable. The tightly coupled array (TCA) mitigates this bilateral radiation with the inclusion of a ground plane at the expense of increased frequency dependence. Such frequency dependence can be balanced with mutual capacitive coupling [12], i.e., the TCA is realized by an *almost* CA of dipoles with a backing reflector. With the advent of the CSA, and the derivative CA and TCA, the antenna bandwidth is governed by finite dipole geometries and feed networks.

Considerable work has been done to develop the electronic feed networks commonly associated with ultrawideband (UWB) arrays. Notably, most UWB elemental radiators, e.g., spirals, tapered slots, and bowties, operate under balanced feeding, as unbalanced feeding produces unequal current magnitudes along the dipole arms that manifest as an undesired standing wave (resonance) between adjacent arrayed elements.

Manuscript received April 15, 2020; revised August 6, 2020; accepted December 5, 2020. Date of publication January 25, 2021; date of current version August 4, 2021. This work was supported by Dr. R. Nelson, AFRL, under Contract FA8650-17-C-5413. *(Corresponding author: Victoria A. Carey.)*

Victoria A. Carey, Shouyuan Shi, and Dennis W. Prather are with the Department of Electrical and Computer Engineering, University of Delaware, Newark, DE 19716 USA (e-mail: vcarey@udel.edu; sshi@udel.edu; dprather@udel.edu).

Matthew R. Konkol, Andrew J. Mercante, Kevin Shreve, Andrew A. Wright, and Christopher A. Schuetz are with Phase Sensitive Innovations, Inc., Newark, DE 19711 USA (e-mail: konkol@phasesensitiveinc.com; mercante@phasesensitiveinc.com; shreve@phasesensitiveinc.com; wright@breakphasesensitiveinc.com; schuetz@phasesensitiveinc.com).

Color versions of one or more figures in this article are available at https://doi.org/10.1109/TAP.2021.3052340.

Digital Object Identifier 10.1109/TAP.2021.3052340

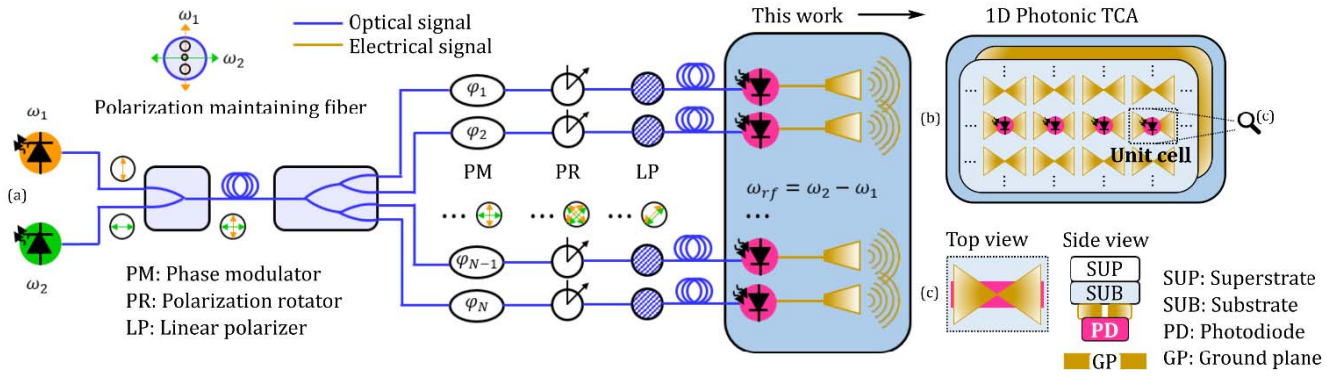


Fig. 1. Transmitting RF photonic phased array system overview illustrating (a) from left to right, a two-laser optical beamforming network driving a 1-D photonic TCA antenna, (b) ideal case for the array in this work with the unit cell indicated, and (c) top and side views of the unit cell in (b). Illustrations are not to scale.

This detrimental effect typically occurs near midband and is referred to as common mode resonance, drawing its name from the inherent common mode feed currents present in coaxial transmission lines [18]. Several techniques are employed for common mode suppression, including feed organizers [19], shorting pins [20]–[23], and unbalanced to balanced transformers, i.e., *baluns* [24]–[27]. The latter also serve as matching networks that improve overall antenna bandwidth but at the expense of cost, complexity, and increased SWaP. In addition, electronic feed networks become increasingly difficult to implement in multioctave phased arrays operating at mmW frequencies due to bulky feed lines, narrowband local oscillators, and mixers that constrain integration density, increase SWaP, and are fundamentally limited by frequency-dependent losses.

The limitations of electronic feed networks for mmW phased arrays can be overcome by an alternative method that uses optically fed photodiodes for array excitation. This photonic approach capitalizes on balanced feeding provided by photodiode sources and direct multioctave RF signal generation provided by optical downconversion [28]–[32]. Fig. 1 illustrates the proposed RF photonic phased array system: a TCA of dipoles with photodiode current sources [Fig. 1(b) and (c)] functioning as the mmW transmitter and an array of electrooptic phase modulators with laser diode sources functioning as the optical beamforming network [Fig. 1(a)] [30]. As shown, this system is designed for RF transmission, but the RF photonic approach is not limited to transmitters, e.g., a comparable photonic receiver would replace the downconversion process at the photodiodes with an upconversion process using electrooptic modulators [6]. The trade-off for the photonic approach requiring separate front-end architectures for receive and transmit operation is in its inherent benefits, namely with respect to loss and utility, e.g., using injection seeding. The beamforming network in Fig. 1(a) is capable of continuous, high-fidelity RF signal generation from 500 MHz to >100 GHz [29], thereby making optical feeding suitable for multifunctional RF systems, where operation spanning several octaves is desirable. Furthermore, the optically generated RF signals experience propagation losses on the order of <0.2 dB/km over optical fiber compared with >100 dB/km for propagation over coaxial cable [33], [34]. Paired with its lightweight, this low loss makes optical fiber suitable for long-distance communication, as in "antenna remoting," where antenna apertures and signal processing architectures are in different locations. In addition to broadband signal generation and low loss, another advantage of using optics to drive RF transmission is the relative bandwidth of any RF signal that is modulated onto an optical signal. A 300-GHz RF carrier constitutes 0.16% of an optical carrier at 1550 nm (~193 THz), thereby making optical channels suitable for RF carriers in the mmW regime and beyond. Moreover, the all-dielectric design of the optical fiber also provides a resistance to electromagnetic interference as an inherent benefit of optical feed networks.

The pairing of an optical feed with an UWB antenna bypasses the fundamental limitations of electronic feeding and places the bulk of the system limits on the performance of transducers, such as photodiodes and electrooptic modulators, and on their integration into the RF photonic system. Accordingly, integration of high-power photodiodes with an UWB transmitter and demonstration of mmW phased array operation using an optical feed network are the focus of this work. Previous work introduces photonic CA antenna design [35] and realizes a low-profile photonic CA exhibiting 4:1 bandwidth with operational frequencies from 5 to 20 GHz [36]. This CA design is then applied to a superstrate-enhanced TCA exhibiting 6:1 bandwidth with operational frequencies from 3.5 to 21 GHz [37]. In this work, the established photonic TCA design approach is implemented in a lower profile package and tailored to support mmW operation upward of 60 GHz. To that end, a direct bonding technique for photodiode integration with the dipole array is also explored to provide insight toward scalable integration solutions.

## II. mmW Photonic TCA Design

A 1-D implementation of the ideal photonic TCA is illustrated in Fig. 1(b). As shown, the 1-D implementation is defined by the placement of the active elements along a single line. In addition, apart from photodiode current sources, the ideal photonic TCA is identical to that of a traditional electronic TCA—namely, a doubly infinite dipole array suspended in free space and backed by a ground plane. Therefore,

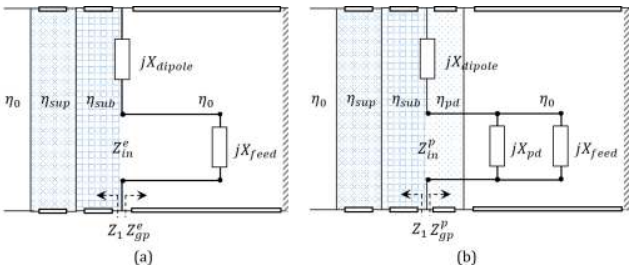


Fig. 2. Equivalent circuit models. (a) Electronic TCA. (b) Photonic TCA.

to model the photonic TCA, we begin by using theoretical methods established for the electronic TCA.

### A. Circuit Model

The equivalent circuit models for the electronic TCA and the photonic TCA are shown in Fig. 2(a) and (b), respectively. For the electronic TCA, the ground plane is modeled as a short-circuited transmission line, i.e., a "shorted stub," that adds a reactance

$$Z^e_{gp} = j\eta_0 tan\left(\beta h_{gp}\right) \tag{1}$$

where $\eta_0$ is the impedance of free space, $\beta$ is the spatial frequency $2\pi/\lambda$, and $h_{gp}$ is the ground plane height, i.e., the distance between the ground plane and the dipole array. However, as shown in Fig. 1(c), the photonic TCA in this work includes the substrate of the photodiode directly integrated to the dipole array and between the dipole array and the ground plane. As shown in Fig. 2(b), the reactance contributed by the photodiode substrate is accounted for with an additional transmission line segment. Assuming a lossless photodiode substrate, the ground plane reactance for the photonic TCA then becomes

$$Z^p_{gp} = \eta_{pd}\frac{Z^e_{gp} + j\eta_{pd}tan\left(\beta_{pd}h_{pd}\right)}{\eta_{pd} + jZ^e_{gp}tan\left(\beta_{pd}h_{pd}\right)} \tag{2}$$

where $\eta_{pd}$ is the impedance of the photodiode substrate material, $\beta_{pd}$ is the spatial frequency inside the photodiode substrate material, and $h_{pd}$ is the height, i.e., thickness of the photodiode substrate. The impedance looking toward the superstrate, i.e., $Z_1$, is determined in a similar fashion, assuming lossless lines and transmission lines in series. Once $Z_1$ and $Z_{gp}$ are determined, these impedance values are placed in parallel with each other and with the reactance values contributed by the antenna [12]. For the electronic TCA, the total input impedance is [38]

$$Z^e_{in} = \left(Z_1||Z^e_{gp} + jX_{dipole}\right)||jX_{feed} \tag{3}$$

where $X_{dipole}$ is the reactance contributed by the dipole arms and $X_{feed}$ is the reactance contributed by the separation between the dipole arms at their feed points. Like the addition of the photodiode substrate to (1) to find (2), the total input impedance of the photonic TCA includes the reactance contributed by the photodiode source. As shown in Fig. 2(b), the reactance contributed by the photodiode is accounted for with an additional reactance in parallel with the dipole array, i.e., between the dipole feed points, and results in a total input impedance

$$Z^p_{in} = \left(Z_1||Z^p_{gp} + jX_{dipole}\right)||jX_{feed}||jX_{pd} \tag{4}$$

where $X_{pd}$ is the reactance contributed by the photodiode.

TABLE I
SIMULATION PARAMETERS AND VALUES

| Symbol | Parameter | Value (mm) |
|---|---|---|
| $l_{x,y}$ | unit cell size | 1.870 |
| $w_g$ | coupling gap | 0.225 |
| $w_d$ | dipole width | 1.300 |
| $l_{fg}$ | feed gap | 0.100 |
| $l_{fw}$ | feed width | 0.020 |
| $l_{fl}$ | feed length | 0.050 |
| $w_{pd}$ | photodiode width | 0.500 |
| $w_b$ | bias line width | 0.050 |
| $h_{sup}$ | superstrate height | 1.500 |
| $h_{sub}$ | substrate height | 0.250 |
| $h_{pd}$ | photodiode height | 0.220 |
| $h_{gp}$ | ground plane height | 1.100 |

### B. 3-D Model

A 3-D full-wave electromagnetic analysis using Ansys High-Frequency Structure Simulator (HFSS) is achieved in conjunction with the circuit model in Fig. 2(b). By grouping the right side of (4) into a single term, it can be rewritten as

$$Z^p_{in} = Z_a||jX_{pd} \tag{5}$$

where $Z_a$ is the antenna impedance. Assuming the antenna and the photodiode impedances may be considered separately, the unit cell architecture is modeled in HFSS using periodic boundary conditions (PBCs) in the plane of the array, an infinite perfect electric conductor (PEC) at the ground plane, and a radiation boundary condition (RBC) in the direction of the superstrate. To simulate the photodiode current sources, terminal excitation is used with a lumped port between the dipole feed points. Fig. 3 shows the HFSS unit cell that was simulated with boundary conditions, port excitation, and simulation parameter definitions indicated. The corresponding simulation parameter values are given in Table I. Fig. 3(a) also includes an overlay of the circuit representation from Fig. 2(b). Using the unit cell, the complex antenna impedance is determined in HFSS. Once the antenna impedance is known, the photodiode impedance is considered. To simplify the analysis, the photodiode impedance is assumed to be a function of its junction capacitance only, i.e., it has a reactance given by

$$X_{pd} = \frac{1}{\mathrm{j}\omega C_j} \tag{6}$$

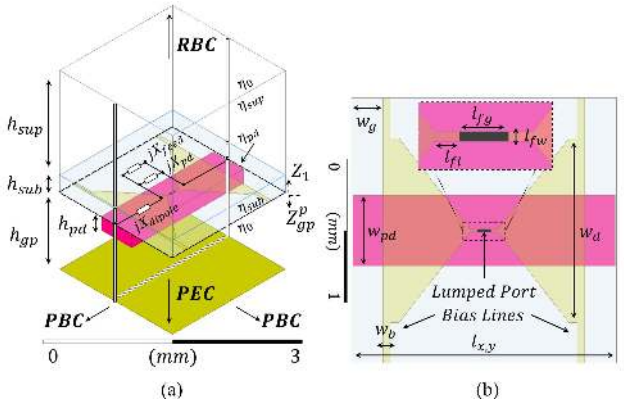


Fig. 3. HFSS unit cell. (a) Perspective view and (b) top view showing boundary conditions, lumped port, and device geometry corresponding to simulation parameters given in Table I. Also illustrated in (a) is an overlay of the equivalent circuit from Fig. 2(b).

where $C_j$ is the junction capacitance; the junction capacitance used here is 47 pF [39]. With the impedance of the photodiode, the total input impedance is determined.

The simulated reactance of the photodiode (dotted), $X_{pd}$, the antenna (black), $X_a$, and the total input impedance of the photonic TCA (blue), $X_{in}$, using (5) and (6) and the values in Table I are all shown in Fig. 4(a). As shown, the gap between dipole arms flattens both the antenna response and the overall input impedance at "low" frequency (near 15 GHz). At "high" frequency, the antenna becomes increasingly inductive as it approaches the natural frequency of its dipoles (near 65 GHz), but the overall input impedance is flattened by the photodiode capacitance as it approaches its *RC*-limited bandwidth. Fig. 4(b) also shows the calculated ground plane impedances using (1) and (2) and an effective photodiode height of $h_{pd} * \left(w_{pd}/l_{x,y}\right)$. As shown, the presence of the high-dielectric photodiode substrate has a significant impact on the impedance of the ground plane. With the photodiode substrate considered, the desired inductive behavior below midband and capacitive behavior above midband is achieved, i.e., the effective ground plane height is near $\lambda_{mid}/4$, a common design approach for broadband planar dipole arrays [12], [40]. The idea behind this design approach is based upon the typical features of a TCA; namely, the low-frequency capacitance introduced by mutual coupling and the high-frequency inductance provided by dipole radiators. Bandwidth is maximized by designing the inductive and capacitive regions of the key components, e.g., the ground plane and the photodiode, to coincide with the capacitive coupling and dipole inductance, respectively. These effects are illustrated in Fig. 4(a).

Once the impedance of the system is determined, the output power must be determined. Using Fig. 1 and ignoring phase shifts due to mechanical and thermal fluctuations in the optical fibers, phase shifts due to the phase modulators, and losses or gains incurred along the fiber feed network, and assuming pure sinusoidal optical sources, the total optical field incident on the photodiode is given by [30], [31]

$$E_{inc} = \frac{\sqrt{2}}{2}\left[E_1 e^{j(\omega_1 t+\beta_1 l)} + E_2 e^{j(\omega_2 t+\beta_2 l)}\right] \tag{7}$$

where $E_1$ and $E_2$ are the optical field peak amplitudes corresponding to $\omega_1$ and $\omega_2$, respectively, $\beta_1$ and $\beta_2$ are the spatial frequencies in the optical fiber corresponding to $\omega_1$ and $\omega_2$, respectively, and $l$ is the length of the optical fibers (assuming equal lengths for $\omega_1$ and $\omega_2$). The factor of $\sqrt{2}/2$ is due to the fields undergoing 45° polarization rotation and subsequent linear polarization filtering. The photodiode generates an alternating photocurrent proportional to the incident optical power, i.e., proportional to the square of the modulus of the incident field in (7), as

$$I_{pd} = \Re H P_{opt} \propto \Re H \frac{|E_{inc}|^2}{2\eta} \tag{8}$$

where $\eta$ is the wave impedance, $\Re$ is the responsivity of the photodiode under single-laser illumination, $P_{opt}$ is the incident optical power, and $H$ is the frequency response of the photogenerated current. This photocurrent frequency response is approximated as [41]

$$H \cong \frac{1 - e^{j\omega\tau}}{j\omega\tau} \tag{9}$$

where $\tau$ is the transit time of the carriers traversing the junction. This approximation can be understood as a phase delay among photogenerated carriers under the assumptions of uniform illumination, 100% internal quantum efficiency, and constant carrier velocity. These assumptions allow the use of a constant for the transit time in (9); the transit time used here is 5 ps [39]. Expanding the squared modulus of (7) in (8) gives

$$I_{pd} \propto \frac{\Re H}{4\eta} \times \left[E_1^2 + E_2^2 + 2E_1E_2 cos\left(\omega_{rf}t + \phi_{rf}\right)\right] \tag{10}$$

where $\omega_{rf} = \omega_2 - \omega_1$ and $\phi_{rf} = l(\beta_2 - \beta_1)$. Since this photocurrent is driving an antenna, the dc terms are inherently filtered out, and the photocurrent at the antenna is

$$I_{rf} \propto \frac{\Re H E_1 E_2}{2\eta} \cos\left(\omega_{rf}t + \phi_{rf}\right). \tag{11}$$

The time-averaged output power across the load, i.e., the antenna, will follow this photocurrent as:

$$P_{out} = \langle |I_{rf}|^2 \rangle R_{in}^p \tag{12}$$

where $R_{in}^p$ is the total input resistance, i.e., the real part of $Z_{in}^p$ in (5).

It is convenient to express the output power as a function of the average (dc) photocurrent rather than the alternating (RF) photocurrent, as the dc photocurrent is readily measured. From (10), the dc photocurrent is

$$I_{dc} \propto \frac{\Re}{4\eta}\left(E_1^2 + E_2^2\right). \tag{13}$$

Taking the ratio of the time-averaged squared RF photocurrent and the squared direct photocurrent gives

$$\frac{\langle |I_{rf}|^2 \rangle}{I_{dc}^2} = \frac{1}{2}\left[\frac{2H E_1 E_2}{\left(E_1^2 + E_2^2\right)}\right]^2. \tag{14}$$

Using (14) to rewrite (12) gives

$$P_{out} = \frac{1}{2}\mathrm{H}^2 m^2 I_{dc}^2 R_{in}^p \tag{15}$$

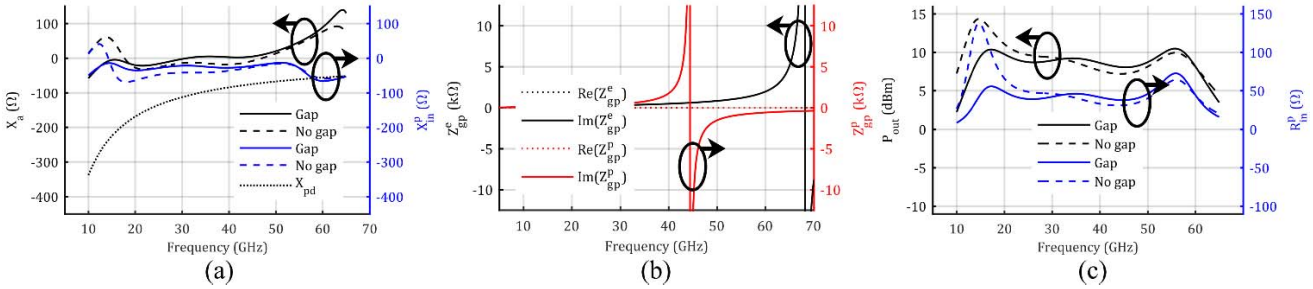


Fig. 4. Simulated frequency response for (a) photodiode, antenna, and input reactance using (5) both with and without a coupling gap; (b) ground plane impedances both with and without photodiode substrate using (1) and (2), respectively; and (c) output RF power using (17) with 20 mA average photocurrent and total input resistance using (5).

where $m$ is the modulation depth and is defined here as $2E_1E_2/\left(E_1^2+E_2^2\right)$. From here, the dc photocurrent and the photodiode frequency response are commonly grouped into a single term that approximately describes the photocurrent present across the load as [39], [41]

$$i_a = I_{dc}H. \tag{16}$$

Substituting (16) in (15) gives the final simplified expression for the output RF power of the antenna

$$P_{out} = \frac{1}{2}m^2|i_a|^2R_{in}^p. \tag{17}$$

The output RF power is an important result for our photonic antenna, as we do not have access to a reflection coefficient measurement, commonly known as S11 in traditional electronic antenna design and characterization. To that end, radiated output power will be the primary simulated and measured quantity and compared against a "50 Ω ideal" that assumes a perfectly matched load to the antenna, i.e., $R_{in}^p = 50\ \Omega$, and a frequency-independent photodiode response, i.e., $H = 1$.

Using (16) and (17), the unit cell in Fig. 3, the values in Table I, 20 mA dc photocurrent, and single port excitation, the output RF power of the photonic TCA is shown in Fig. 4(c) both with and without a coupling gap, in order to provide a direct comparison to the impedances shown in Fig. 4(a). As expected, the output power shorts to the ground plane at low frequency, shorts through the photodiode at high frequency, and peaks at midband due to quarter-wave transformation in the superstrate. For more information on superstrate enhancement, the reader is directed toward [11], [12], [37]. In Fig. 4(c), the balancing effect, previously discussed, between the coupling gap and the ground plane is also apparent in the output power.

### C. Photonic Design Considerations

The peak in output power within our band of interest is not commonly considered detrimental to traditional electronic antennas but is undesirable for photonic antennas due to the saturation behavior of photodiode current sources. For example, photodiodes under small-signal sinusoidal operation can avoid saturation effects by maintaining a minimum bias condition [42], [43]

$$V_{min} \leq -V_t - \frac{I_{dc}}{\alpha}(1+m) - mI_{dc}R_L \tag{18}$$

where $V_{min}$ is the minimum applied reverse bias voltage, $V_t$ is the photodiode "turn-on" voltage, $\alpha$ is an observed quantity that describes space charge screening within the photodiode junction, $m$ is the modulation depth of the signal driving the photodiode, and $R_L$ is the load resistance. Assuming negligible space charge effects, a constant turn-on voltage, and 100% modulation depth, the minimum bias condition becomes a function of dc photocurrent and load resistance. With respect to our antenna, this means that the minimum bias condition of the photodiode will vary with $R_{in}^p$. Since the output power of the antenna follows $R_{in}^p$, as in (17), and as shown in Fig. 4(c), the minimum bias condition of the photodiode will also vary with antenna output power. In an attempt to ensure that the efficiency of the antenna and photodiode remain decoupled across the band of interest, we later define a 3 dB variation in radiated power as our bandwidth metric, contrasting the traditional figure of merit employing a maximum voltage standing wave ratio (VSWR).

The biasing requirements are unique to the photonic TCA as they are required to maintain photodiode linearity with high levels of photocurrent where increases in optical to electrical conversion efficiency and power output have been demonstrated [44]–[47]. With respect to our antenna, this means that the bias lines must be included in the antenna design. Shown in Fig. 3, the bias lines are integrated along the dipole arms. The primary design challenge introduced by the bias lines is preventing induced scan blindness, which can be understood as a destructive resonance that occurs as the effective length of the bias lines approach $\lambda/2$, i.e., they will be resonant at wavelengths defined by

$$\lambda_{res} = \frac{2l_{bias}\sqrt{\varepsilon_{eff}}}{\cos(\theta_{||})} \tag{19}$$

where $l_{bias}$ is the physical length of the lines between neighboring dipoles, $\varepsilon_{eff}$ is the effective permittivity accounting for proximal dielectric media, and $\theta_{||}$ is the scan angle in the plane of the bias lines. Bias line resonance can be avoided or pushed out of band by careful design of $\varepsilon_{eff}$ or $l_{bias}$. The former is heavily influenced by the antenna and photodiode substrates, while the latter is primarily a function of the array sampling.

The array sampling is set by the highest operating frequency to be equal to or less than $\lambda_{min}/2$ [40]. For operation up to 60 GHz, the maximum element spacing is 2.5 mm. However, as in (19), the dipole elements will be electrically lengthened by $\varepsilon_{eff}$ and require oversampling to achieve the high-frequency response their physical length alone would provide. Though oversampling is a solution, it is often undesirable as it increases element count without increasing antenna gain. Oversampling at $0.75\lambda_{min}/2$ was found to be minimal while maintaining the desired antenna bandwidth.

To complement oversampling, which decreases physical lengths like $l_{bias}$ directly, effective lengths can also be minimized by decreasing $\varepsilon_{eff}$, as shown in (19). Since $\varepsilon_{eff}$ is governed mostly by the antenna and photodiode substrates, their respective materials and dimensions play a central role in the design space. The antenna substrate is aluminum nitride (AlN) and the photodiode substrate is indium phosphide (InP). These two materials are not conventionally "good" antenna materials due to their high electrical susceptibilities, e.g., permittivity values of approximately 8.8 and 12.4, respectively, but they are well-known photonic materials. Specifically, InP is used in the photodiode epitaxy and as the photodiode substrate [39], and AlN functions as the photodiode heat sink [48]. In previous work, 1 mm square photodiode chips with thicknesses of 0.65 mm were individually bonded to coplanar waveguides, epoxied to the antenna substrate near the dipoles, and wire bonded to the dipole feeds [35]–[37]. Due to the relatively small volume occupied by the photodiodes, and their placement away from the dipoles, InP substrate thicknesses were inconsequential; however, the optimal tradeoff between bandwidth and fabrication complexity for the AlN substrate thickness was found to be 0.25 mm [37]. For this work, the AlN antenna substrate thickness is kept at 0.25 mm, but the InP photodiode substrates are thinned from 0.65 to 0.22 mm to accommodate their increased volume and proximity to dipole elements. The effect of the photodiode substrate thickness on the frequency response of the array is shown in Fig. 5 for thicknesses of 0.10, 0.30, and 0.65 mm and scan angles of 0°, 15°, 30°, and 45°. As shown, the output power using the original thickness of 0.65 mm fails to remain inside a 3 dB power variation that defines the bandwidth of our photonic antenna both at broadside radiation and at scanning angles of 30°. Also evident from Fig. 5 is that any thickness between 0.10 and 0.30 mm is sufficient to scan angles of 30°; this range of values determined the fabrication tolerance during the photodiode substrate thinning process, to be discussed in Section III, and led to the final thickness of 0.22 mm given in Table I.

### *D. Simulated Antenna Result*

The simulated photonic TCA frequency response and array responses using the unit cell in Fig. 3 and the values in Table I are shown in Fig. 6(a)–(c). Fig. 6(a) shows the frequency response with 20 mA dc photocurrent and single port excitation in the E-plane (top) and H-plane (bottom) for scan angles of 0°, 15°, 30°, and 45°. The changes in output RF power with scan angle can be likened to the effective shortening of the array geometry in the E-plane and the effective lengthening of the array geometry in the H-plane, i.e., the input impedance of the array at each frequency varies as in (5) where $Z_a$ varies with scan angle as [14], [17]

$$Z_a(\theta) = Z_a(0)\left[\frac{dx}{dy}\frac{\cos(\theta)}{1 - sin^2(\theta)sin^2(\varphi)}\right] \tag{20}$$

where $\theta$ is the scan angle, $dx/dy = \cos(\theta)$, and $\varphi = 0°$ and 90° for E- and H-plane scanning, respectively. As shown in Fig. 6(a), the proposed design achieves a 3 dB radiated power bandwidth of 4.6:1 across 13–60 GHz at broadside. To improve broadside bandwidth upward of 6:1, further optimization of $\varepsilon_{eff}$ would yield promising results, e.g., using a thinner AlN antenna substrate, at the expense of fabrication complexity, or substituting AlN with a lower dielectric Rogers or diamond substrate, at the expense of lower power handling and cost, respectively. Away from broadside, the design maintains a 3 dB radiated power bandwidth near 4:1 out to 30° scanning in the E- and H-plane, i.e., the plane perpendicular and parallel with the photodiode bias lines, respectively. Comparing the response of the array in the E-plane to the response in the H-plane, the effect of the bias lines is clear; since the H-plane is in the plane of the bias lines, their effective lengths become lengthened by $\theta_{||}$ as indicated in (19). As a result, a blue-shifted destructive resonance can be seen with increasing scan angle.

Comparing the broadside and scanning performance of the proposed mmW photonic TCA design with its electronic counterparts reported in literature, it is important to distinguish between the contrasting figures of merit. The 3 dB bandwidth metric used here is comparable to a VSWR $< 1.4$, while the state-of-the-art bandwidths reported for traditional electronic arrays are against VSWRs of $<2$ and commonly $<3$ that are equivalent to power variations of 6 and 9.5 dB, respectively. Considering a 6 dB variation, the proposed array approaches 6:1 bandwidth at broadside and maintains 4.5:1 bandwidth out to 30° scan angles in both planes; to the best of our knowledge, these are the highest broadside and scanning bandwidths reported for an antenna array operating at these frequencies [23], [49]–[51].

The simulated photonic TCA array behavior using multiple ports and perfectly matched loads is shown in Fig. 6(b) and (c). Fig. 6(b) shows the simulated directivity for a $1 \times 9$ array operating at 60 GHz in the E-plane (top) and H-plane (bottom) for scan angles of 0°, 15°, 30°, and 45°. As shown, beam steering occurs in the E-plane, and the response varies with scan angle, reflecting the influence of impedance variations as expected. Fig. 6(c) shows the simulated directivity as a function of frequency (top) and element count (bottom). The frequency comparisons are for a $1 \times 9$ array operating at 20, 40, and 60 GHz, and the element count comparisons are for $1 \times 1$, $1 \times 3$, and $1 \times 9$ arrays operating at 60 GHz. Since the array includes an infinite ground plane, the E- and H-plane patterns are shown on the same plot but offset by 180°. As shown, the simulated array exhibits beam narrowing and increasing peak directivity with increasing frequency and element count, as expected. The simulated peak directivities for the curves in Fig. 6(c) are also given in Table II.

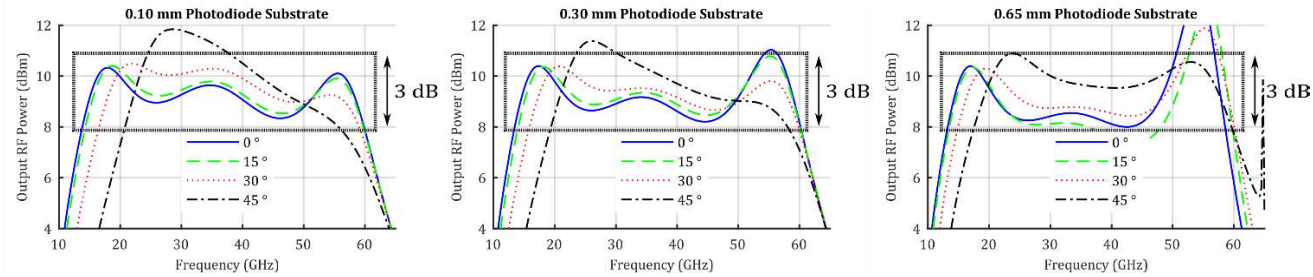


Fig. 5. Simulated frequency response as a function of photodiode substrate height, $h_{PD}$. The 50 Ω ideal is 10 dBm.

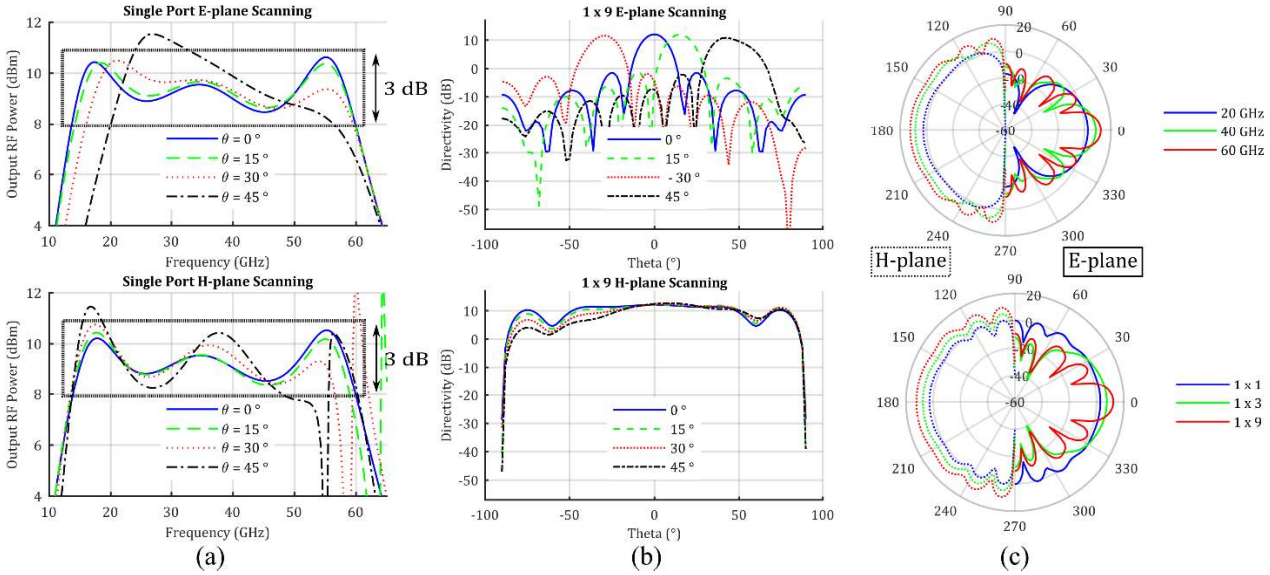


Fig. 6. Design results. (a) Frequency response for various scan angles in the E-plane (top) and H-plane (bottom). (b) Directivity of $1 \times 9$ array for various scan angles in the E-plane (top) and H-plane (bottom) for 60 GHz operation. (c) E-plane (solid line) and H-plane (dotted line) radiation patterns (dB) as a function of frequency for a $1 \times 9$ array (top) and as a function of element count for 60 GHz operation (bottom).

TABLE II
SIMULATED PEAK DIRECTIVITIES

| # Elements | Frequency | Peak Directivity (dB) |
|---|---|---|
| 1 | 60 GHz | 2.7 |
| 3 | 60 GHz | 7.5 |
| 9 | 60 GHz | 12.3 |
| 9 | 40 GHz | 8.5 |
| 9 | 20 GHz | 2.5 |

## III. ARRAY FABRICATION

The proposed design from Section II is the ideal, infinite antenna, i.e., the planar structure was assumed infinite in extent with port excitations ranging from 1 to 9 to simulate the ideal array response. A finite antenna structure is required for implementation. The proposed finite photonic TCA is illustrated in Fig. 7. As shown in Fig. 7(a), the finite design includes a $1 \times 4$ array of photodiode sources integrated on a $9 \times 12$ array of dipoles with surface mount resistor terminations. It was found in previous work that these termination resistors assisted in the frequency response of the finite array by "spreading out" the current distribution such that an array with resistors approximated an infinite array better than an array without resistors [52]. The finite design also includes the layout for the photodiode bias control. The bias lines terminate at the bottom of the array and are truncated above their corresponding photodiode sources such that they do not supply current to the neighboring termination resistors. Also shown in Fig. 7(a) is a back view [top right of Fig. 7(a)] highlighting the perforated ground plane required for illuminating the photodiodes. The side view in Fig. 7(b) illustrates the ground plane, optical input, and RF output. The optical inputs are aligned to the photodiodes through the ground plane, the photodiodes excite a current distribution across the dipole array, and that current then preferentially radiates through the superstrate and into free space.

To implement the proposed finite design, the array fabrication addressed several key objectives: forming the dipole array and bias network; thinning the photodiode substrates and bonding them to their dipole feeds; and optically feeding the photodiodes within the physical design space set by the array sampling. These objectives are divided into the following three

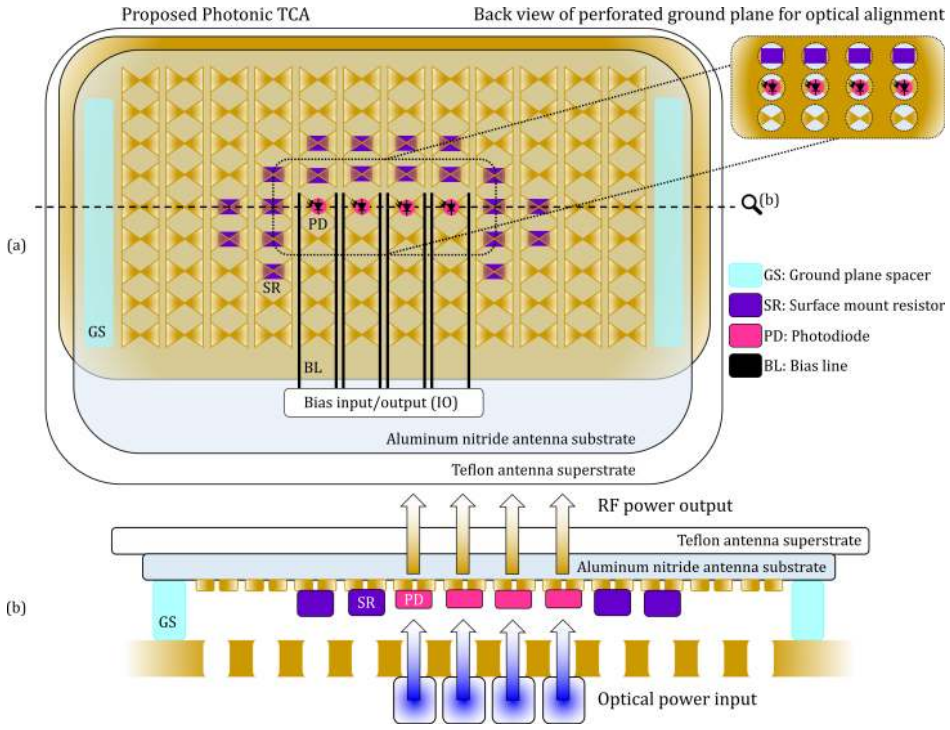


Fig. 7. Finite photonic TCA overview. (a) Top view of proposed design illustrating 1-D array of photodiode current sources, 1-D photodiode bias control, termination resistors, and perforated ground plane. (b) Side view illustrating the cross section at the magnifying glass indicator in (a). Illustrations are not to scale.

sections: antenna substrate preparation, photodiode integration, and optical alignment and packaging.

### *A. Antenna Substrate Preparation*

The antenna dipole array consists of a $9 \times 12$ array of gold (Au) bowtie radiators on a 57 mm square AlN substrate, from MARUWA America Corp., with a thickness of 0.25 mm and was electroplated with standard microfabrication techniques. After substrate cleaning with a 3:1 sulfuric acid to hydrogen peroxide (piranha) mixture, RF sputtering was used to deposit a 4 nm titanium adhesion layer followed by a 100 nm Au seed layer for electrodeposition. Photoresist was spin deposited, exposed, and developed for array pattern transfer. Following subsequent cleaning with an oxygen plasma, the array pattern was electroplated in TechniGold 25 ES RTU solution to a thickness of approximately 4 $\mu$m. After electroplating, the resist, seed, and adhesion layers were removed iteratively in piranha (resist removal), iodine-based Au etchant (seed removal), and piranha (adhesion removal).

Included in the electroplated antenna pattern are the bias lines that terminate to a standard 24 pin ribbon connector. After electroplating, the ribbon connector was epoxied to the substrate for structural support and wire bonded to the corresponding terminations. This ribbon connector allows for a simple printed circuit board (PCB) to RS232 network for bias control and dc photocurrent measurement.

### *B. Photodiode Integration*

The photodiodes used to drive the antenna are CC-MUTC photodiodes designed by the University of Virginia for high power and high linearity up to 65 GHz [39]. Mentioned previously, the array performance is limited above midband by the frequency response of the photodiode and the natural frequency of its dipole elements. To extend this natural frequency without extensive oversampling, the effective permittivity is lowered by decreasing the thickness of proximal dielectric media, i.e., by thinning the photodiode substrates.

Mechanical lapping and polishing were used to thin the photodiode substrates from approximately 0.65 to 0.22 mm. A series of water-based alumina slurries with particle diameters ranging from 20 to 3 $\mu$m were used on a steel platen to remove the first 0.4 mm. The final 0.03 mm was removed with a 3 $\mu$m water-based diamond suspension on a felt pad. Once thinned, the photodiode substrates were polished further with 0.1 and 0.06 $\mu$m silica suspensions to attain optical finishes for improved antireflection response during illumination [53].

Thinning the photodiode substrate compensates for their increased influence on the effective permittivity and enables the bonding approach investigated in this work. This approach is not ideal, i.e., wafer scale, but is a practical first step when considering 1-D array implementation. Accordingly, a 1-D array of photodiode sources was integrated by sequential flip-chip bonding, as shown in Fig. 8(a). Flip-chip bonding achieves placement tolerances $<1$ $\mu$m, as is required to ensure accurate alignments between photodiode contacts and dipole feeds. Infrared images of actual bonds between photodiode chips and their dipole feeds are shown in Fig. 8(b) and (c). The bond was formed using ultrasound assisted Au–Au thermocompression bonding at 300 °C with a 400 g bond load and 60 s of bond time. After bonding, adjacent inactive dipoles in the vicinity of the active photodiodes were terminated with

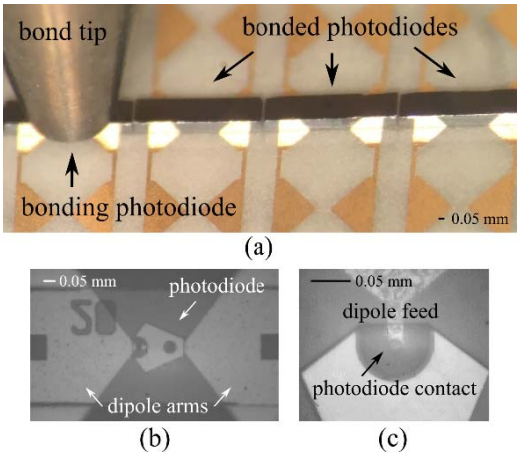


Fig. 8. 1-D photodiode integration. (a) White light image showing *in situ* bonding of photodiode to electroplated dipole array. (b) and (c) Infrared images showing accurate bonds of photodiodes to dipole feeds.

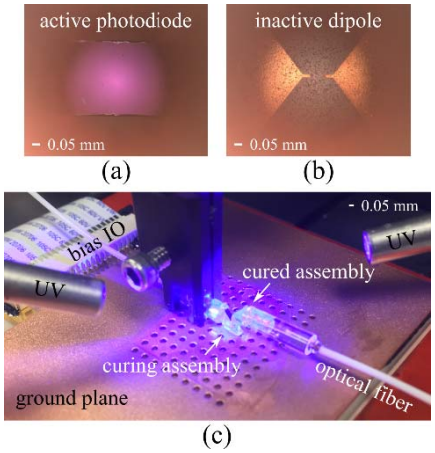


Fig. 9. White light images of ground plane integration and optical alignment. (a) and (b) Rough alignment of ground plane to photodiode and dipole, where the blurry brown outline is the actual, out of focus, ground plane. (c) *In situ* curing of the optical assembly for the second aligned channel.

resistors to improve the finite effects on current distribution, as shown in Fig. 7 [37], [52]. Although 50 Ω resistors are approximately ideal, as shown by the total input resistance of the array in Fig. 4(c), a combination of 100 and 200 Ω resistors were used as they were readily available; this resistor combination is included in the finite simulation result and is expected to have a marginal effect on the array behavior.

With four adjacent photodiodes successfully integrated onto the antenna substrate, the ground plane was added. As indicated by (1)–(5), the spacing between the ground plane and the dipole array is critical for maintaining the intended frequency response of the antenna. To ensure accurate ground plane height, a 3-D printed ABS-like polymer spacer was used with a thickness of 1.1 mm. The spacer was adhered to the antenna substrate and the ground plane was epoxied atop the spacer. A machined copper ground plane was used with perforations of 0.4 mm radii and 1.87 mm periodicity. Once a rough alignment was achieved using a white light microscope, as shown in Fig. 9(a) and (b), the photodiodes were excited on an optical alignment stage, one-by-one, while monitoring the output dc photocurrent via the bias network. Using the dc photocurrent, the ground plane position was adjusted until all four photodiodes were responsive.

### C. Optical Alignment and Packaging

The active photodiode sources were excited through the perforated ground plane by optical fibers terminated with gradient-index (GRIN) lenses and right-angle prisms. Each channel was aligned on an optical alignment stage, like the process for aligning the ground plane, where the dc photocurrent was monitored via the bias network. Based on input optical power and output dc photocurrent, the responsivity of each photodiode was determined in amperes per watt (A/W) with a target responsivity of approximately 0.23 A/W, i.e., 50% of the reported maximum [39]. This integration technique of exciting the photodiodes at half responsivity serves to improve their power handling and longevities due to a more uniform distribution of generated carriers across the junction at the

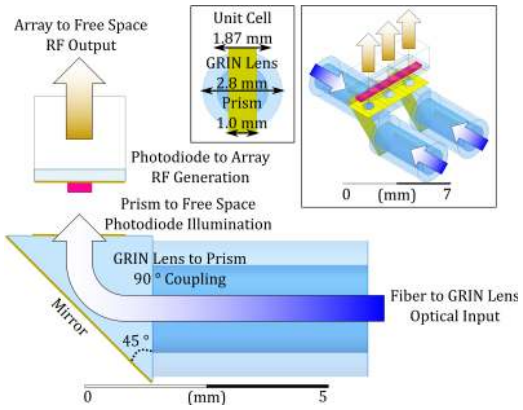


Fig. 10. Side view of signal flow through unit cell from fiber input to array output. Left inset: comparison of optical component dimensions with unit cell dimensions. Right inset: perspective view of 1 × 3 array implementation.

expense of decreased optical to electrical power conversion efficiency (PCE). Once a responsivity near target was reached, the optical assemblies were secured using UV curable Norland Optical Adhesive 61, as shown in Fig. 9(c). Also shown in Fig. 9(c) is a weaving technique that was implemented to accommodate the use of commercially available optical components, thereby avoiding additional complexities associated with custom lens design. Initially, the use of commercial components was prohibited by the array spacing in the antenna design, e.g., the array spacing is 1.87 mm and the diameter of the lens assemblies is 2.8 mm. However, by alternating the input directions, i.e., "weaving," the integration became limited by the widths of the prisms, which were diced to widths of 1.0 mm. Fig. 10 shows the optical components integrated with the unit cell from Fig. 3. As shown, dicing the prisms and weaving the optical feeds provided an integration solution within the design space of the antenna that also used off-the-shelf optical components.

During optical alignment, it was determined that one of the photodiodes had lost its electrical connection with its dipole. The temperature cycling during the flip-chip bonding

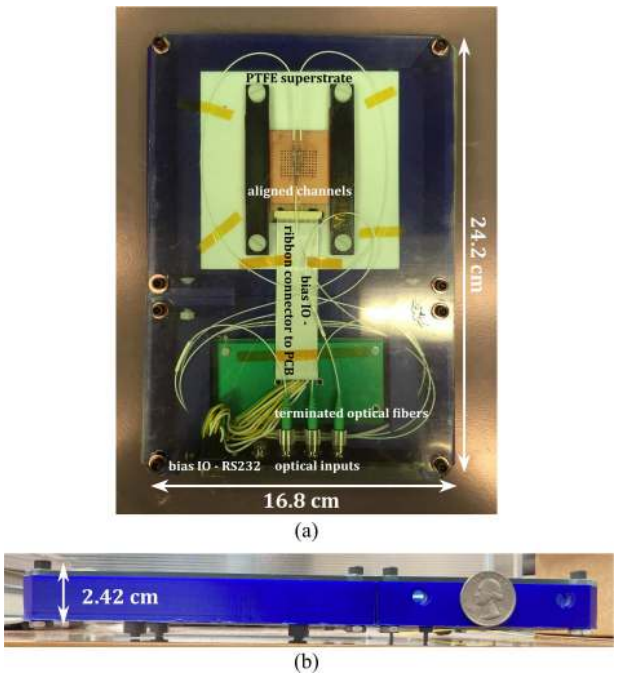


Fig. 11. Integrated and packaged mmW photonic TCA. (a) Top and (b) side views showing dimensions of 24.2 (L) × 16.8 (W) × 2.42 (H) cm.

and flexing of the thin (0.25 mm) substrate was suspected to be the cause of failure, but the remaining three channels did not fail after being subjected to the same processing. Therefore, it is likely that the failure was due to a weak flip-chip bond that was more susceptible to failure than the others, given the same mechanical stresses. Losses of channels due to the failure of a flip-chip bond is undesirable and reflects a drawback to this integration method. For future implementations, monolithic integration should be considered. Despite the loss of a channel, a $1 \times 3$ array remained.

With the remaining three channels optically aligned, the TCA substrate, bias network, ground plane, and optical assembly were packaged inside a 3-D printed housing with the addition of a 1.50 mm polytetrafluoroethylene (PTFE) superstrate. The completed antenna integration is shown in Fig. 11. As shown, the use of right-angle prisms provided a low-profile design. Given a midband wavelength of 8.56 mm, the unpackaged height of the array was $<0.8\lambda_{mid}$ and the packaged height was $<3\lambda_{mid}$. After packaging, the average responsivity was $0.16 \pm 0.04$ A/W with values ranging from 0.12 to 0.18 A/W, as given in Table III. As given, the responsivities decreased from approximately 0.23 to 0.16 A/W during the curing process—a 30% loss. This loss is undesirable as it increases the optical power budget and reflects a drawback to this integration method. For future implementations, on-chip waveguide feeds or optical fiber lenslet arrays should be considered [54]–[56].

## IV. Antenna Characterization

To generate an RF signal, the photodiodes require an optical *difference* signal, e.g., two lasers with frequencies separated by an amount equal to the target RF drive frequency. This is commonly referred to as "optical heterodyning," an approach that is prevalent in photodiode characterization [39], [48], [57]. This heterodyning approach has been coupled with sideband injection locked lasers to provide a low phase noise, broadly tunable optical source capable of generating the high-frequency, high-purity RF signals desired for beamforming with a mmW TCA [29]. In addition to the RF frequency, the phase shifts between active elements are also implemented optically, as illustrated in Fig. 1. For brevity, the details of this photonic phase feed network are omitted but can be found in [29], [30], and [36].

TABLE III
Measured Channel Responsivities After Packaging

| Channel # | Responsivity (A/W) |
|---|---|
| 1 | 0.12 |
| 2 | 0.17 |
| 3 | 0.18 |

The antenna characterization setup is illustrated in Fig. 12 using the beamforming network in Fig. 1. Although the beamforming network illustrated omits the injection locking approach in the actual beamforming network used to drive the array, it clearly illustrates the detection method of our photonic receiver. As shown, a standard gain horn antenna (SGHA) was used to receive the RF signal transmitted from the device under test (DUT) – the $1 \times 3$ fabricated RF photonic TCA. Once the signal from the DUT is received, it undergoes an electrooptical upconversion/downconversion process using the optical carriers from the beamforming network that were used to define the transmitted RF signal. In the beamforming network, the RF signal is shifted by an intermediate frequency (IF) which defines the ideal transmitted signal frequency as

$$\omega_{rf} = \omega_2 - \left(\omega_1 + \omega_{if}\right) \tag{21}$$

where $\omega_{rf}$ is the radial frequency transmitted by the DUT, $\omega_1$ and $\omega_2$ are the radial frequencies emitted from the laser diode sources, and $\omega_{if}$ is the radial frequency of the IF introduced by the QPSK modulator. Upon reception by an SGHA, the RF signal is amplified by an UWB low noise amplifier (LNA) and upconverted by a null-biased MZM with an optical carrier from the laser diode source emitting $\omega_2$. This upconversion process yields sidebands of around $\omega_2$ that are offset in frequency by $\omega_{rf}$ and proportional in magnitude to the received signal multiplied by a constant that describes the gain of the SGHA, the gain of the UWB RF LNA, and the efficiency of the upconversion process through the MZM. After upconversion, the received signal is combined with the optical carrier from the laser diode source emitting $\omega_1$ and mixed on a "low"-frequency photodiode. Ignoring higher order mixing terms, the following frequency components are created

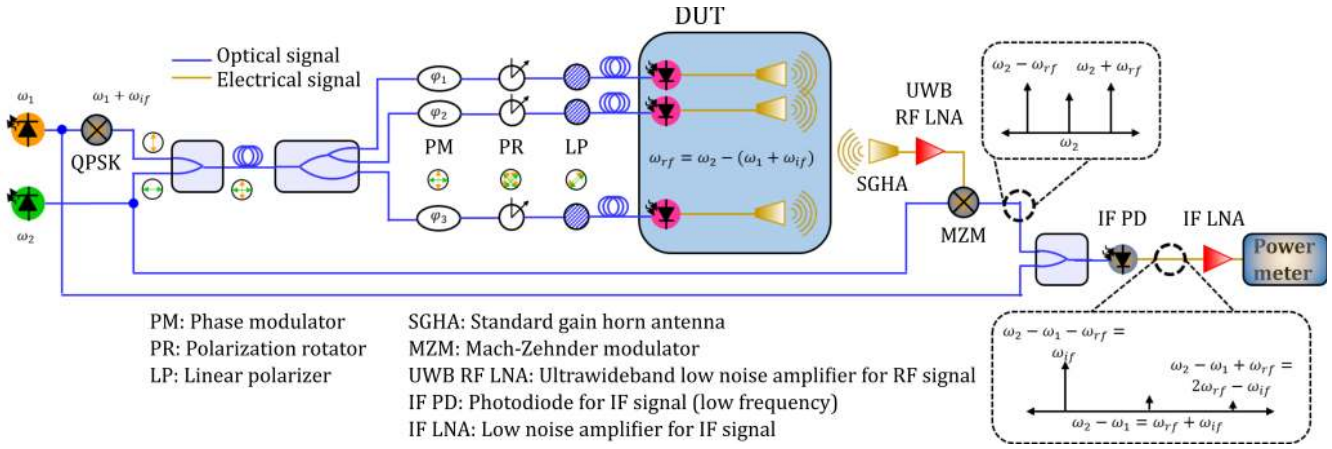


Fig. 12. Transmitting RF photonic TCA characterization overview, from left to right: beamforming illustration from Fig. 1 with the addition of a QPSK modulator and an updated transmitter layout to reflect the DUT; UWB RF photonic receiver comprised of an SGHA (swappable) and an electrooptical upconversion/downconversion process to mix the received RF signal down to an IF signal that is then measured with a power meter. Illustrations are not to scale.

during downconversion at the IF photodiode:

$$\omega_{s1} = \omega_2 - \omega_1 - \omega_{rf} = \omega_{if}, \tag{22}$$

$$\omega_{s2} = \omega_2 - \omega_1 = \omega_{rf} + \omega_{if}, \tag{23}$$

$$\omega_{s3} = \omega_2 - \omega_1 + \omega_{rf} = 2\omega_{rf} - \omega_{if}, \tag{24}$$

$$\omega_{a1} = \omega_2 + \omega_1 - \omega_{rf} = 2\omega_1 + \omega_{if}, \tag{25}$$

$$\omega_{a2} = \omega_2 + \omega_1, \tag{26}$$

$$\omega_{a3} = \omega_2 + \omega_1 + \omega_{rf} = 2\omega_2 - \omega_{if} \tag{27}$$

where $\omega_{s1}$, $\omega_{s2}$, and $\omega_{s3}$ are the frequencies due to the subtraction of $\omega_1$ from the upconverted signal, and $\omega_{a1}$, $\omega_{a2}$, and $\omega_{a3}$ are the frequencies due to the addition of $\omega_1$ to the upconverted signal. Although there are six fundamental components in the frequency spectrum following the downconversion at the photodiode, the IF is designed such that the photodiode conversion efficiency for (23)–(27) is prohibitive, i.e., the signals present at these frequencies may be considered negligible. Fig. 12 illustrates the approximate frequency spectrum before and after downconversion. After downconversion, the signal is amplified and yields a signal that is centered at the IF and proportional in magnitude to the received signal multiplied by a constant that describes the gain of the photonic receiver, which includes the gain of the SGHA, the gain of the LNA, the conversion efficiency of the upconversion and downconversion processes, and the gain of the IF LNA. This magnitude is then detected with a power meter and used to characterize the performance of the DUT at various operating frequencies across the band of interest.

Since the operational frequencies of the array encompass multiple communication bands, measurements were taken to accommodate the bandwidths of available SGHAs. These banded measurements included the frequency ranges 12–18, 26–40, and 40–60 GHz. At each measurement frequency, the SGHA was placed in the far-field of the DUT, at a distance of approximately 1.524 m, and the output power from the array was determined using Friis' transmission formula [4]

$$P_{tx} = P_{rx} - G_{rx} - G_{tx} + FSPL \tag{28}$$

where $P_{tx}$ is the power transmitted, $P_{rx}$ is the power received, $G_{rx}$ is the gain of the photonic receiver illustrated in Fig. 12 and described previously, $G_{tx}$ is the gain of the transmitter (DUT), and $FSPL$ is the free-space path loss. At each frequency, $FSPL$ was determined by the distance between the transmitter and receiver [40], $G_{tx}$ was determined by HFSS using the unit cell in Fig. 3 and the values in Table I with $1 \times 3$ port excitations, and $G_{rx}$ was determined by calibration measurements using the substitution method: received power was measured from a transmitting SGHA driven by a signal generator at each frequency and then used to normalize the data measured with the DUT in place of the reference SGHA.

The measured frequency response of DUT at 5 mA dc photocurrent per channel (15 mA total) and an applied reverse bias voltage of 3 V per channel from 10 to 60 GHz is shown in Fig. 13(a). As shown, measured data matches well to simulation with an outlier at 60 GHz. Since the discrepancy at 60 GHz is isolated and above midband, it was likely a result of one or more of the following: poor injection locking, measurement uncertainty in the receiver power table that determined the receiver gain, and optical to electrical PCE degradation among the photodiodes due to capacitive or transit time roll-off [45], [58]–[60]. This roll-off was included in the simulation using junction capacitance and transit times for similar photodiodes [39], but these values were not measured directly. Further insight into the behavior of the finite array can be gained by inspecting its input impedance, shown in Fig. 13(b). As shown, the simulated finite array exhibits resonance near 12, 18, and 22 GHz. This resonant behavior was reflected in measured data at 12 and 18 GHz, and the response at 22 GHz was not measured. The resonances seen at 12 and 18 GHz are believed to be the result of the finite extent of the antenna, i.e., a half wavelength at 12 and 18 GHz is comparable to the physical length of the dipole array (approximately 17 mm) and the physical length of the photodiode array (approximately 9 mm), respectively, when considering proximal dielectric effects. Various other differences in the frequency responses shown in Fig. 6(a) for the infinite array

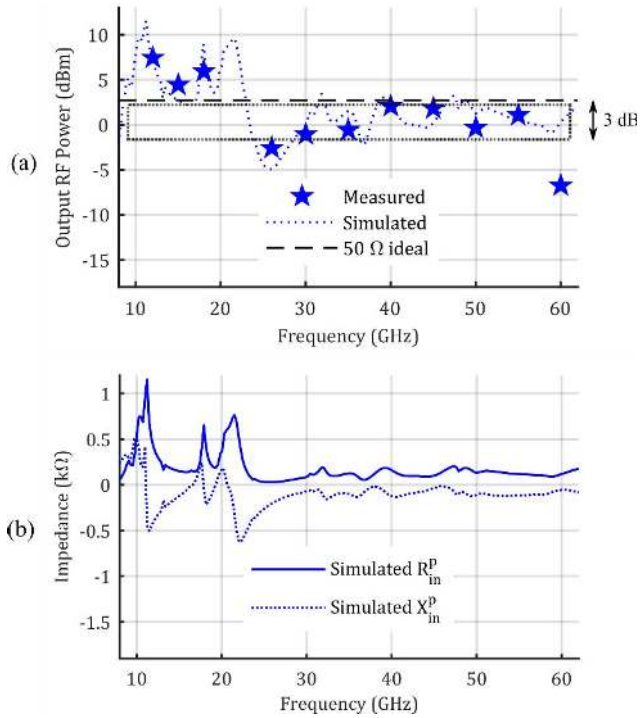


Fig. 13. Frequency response of fabricated array with 5 mA dc photocurrent per channel. (a) Measured (pentagrams) and simulated (lines) output RF power. (b) Corresponding simulated impedance for the finite array with the response shown in (a).

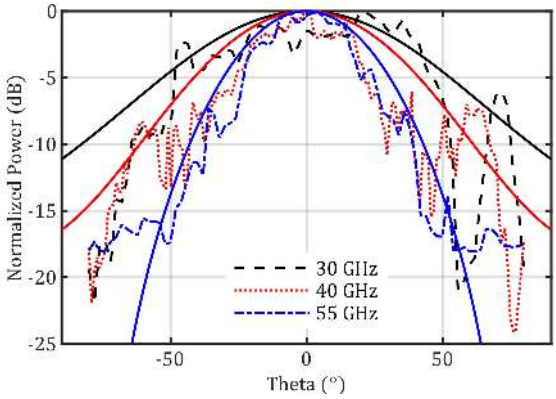


Fig. 14. Normalized radiation patterns of measured (dashed and dotted lines) and simulated (solid lines) array at 30, 40, and 55 GHz.

and Fig. 13 for the fabricated array can be attributed to finite channel count as well as finite aperture effects, e.g., PBCs were applied to the unit cell shown in Fig. 3 to give the responses shown in Fig. 6(a), while perfectly matched layer (PML) boundaries were applied to a truncation of the fabricated structure shown in Fig. 7 to simulate the responses shown in Fig. 13. In addition, a single photodiode source generating 20 mA dc photocurrent gave the simulated responses shown in Fig. 6(a), while three photodiode sources generating 5 mA dc photocurrent each gave the simulated responses in Fig. 13. As such, the ideal output RF power is reduced for the simulated fabricated array (2.73 dBm) versus the simulated infinite array (10 dBm) due to reduced photocurrent. Despite its low photocurrent and finite size and channel count, the fabricated array exhibited a measured 3 dB (VSWR $<$ 1.4) radiated power bandwidth of 1.8:1 across 30–55 GHz with a measured output RF power of 2 dBm at 40 GHz (midband).

Radiation behavior was evaluated by physically rotating the array in the E-plane using a rotation stage while keeping the SGHA receiver position constant. The normalized measured radiation patterns at 30, 40, and 55 GHz from $-85°$ to $+85°$ are shown in Fig. 14. As shown, measured data matches well to simulation with the exception of finite aperture effects, e.g., the finite extent of the ground plane, resulting in beam shape deformation and the early onset of side lobes [61]–[63]. These finite aperture effects also become less apparent with increasing frequency, as expected. Loss of phase calibration between each channel over the course of a scan and multipath interference due to the absence of an anechoic chamber are also potential influencers of the observed discrepancies. Despite these discrepancies, the fabricated array exhibits the expected beam narrowing with frequency and demonstrates effective radiation across its designed bandwidth.

The effective isotropic radiated power (EIRP) was evaluated using

$$\text{EIRP} = P_{tx} + G_{tx} = P_{rx} - G_{rx} + FSPL. \tag{29}$$

The measured and simulated EIRP for the DUT with 5 mA dc photocurrent per channel (15 mA total) is shown in Fig. 15 for 30, 40, and 55 GHz, and an additional EIRP with up to 20 mA per channel (60 mA total) is shown for 40 GHz (midband). Measured values shown at 5 mA were with an applied reverse bias voltage of 3 V per channel and measured values shown above 5 mA were with 5 V per channel. Simulated EIRP was determined using (7) and (8), and the simulated total input impedance of the fabricated array, shown in Fig. 13(b). The 50 Ω ideal is also shown in Fig. 15, which uses (7) and (8), and a 50 Ω total input impedance. As shown, the radiation efficiency of the antenna increases with increasing frequency, i.e., as the frequency approaches $2c/\lambda_{min}$, as shown by the relative offset of each curve from the 50 Ω ideal; this behavior is also observed in the measured EIRP, as expected. The measured EIRP also increased exponentially with increasing photocurrent, as predicted by (17), and matches well to simulation except for the measured values at 40 GHz for photocurrents $\geq$10 mA being greater than their corresponding simulated values. This discrepancy is likely due to inaccuracies in the transit time value used to simulate the frequency response of the photodiodes. The transit time generally varies with electron velocity, and the electron velocity varies with the electric field distribution across the junction [60], [64]. The electric field distribution is a function of the doping, the photocurrent, and the applied reverse bias voltage. As a result, the transit time will also vary with the photocurrent and the applied reverse bias voltage. However, for our analysis, the transit time was treated as a constant, which may have led to erroneous results in the simulated EIRP curves. Since the gain of the fabricated array was not determined directly, the discrepancies in the radiation pattern

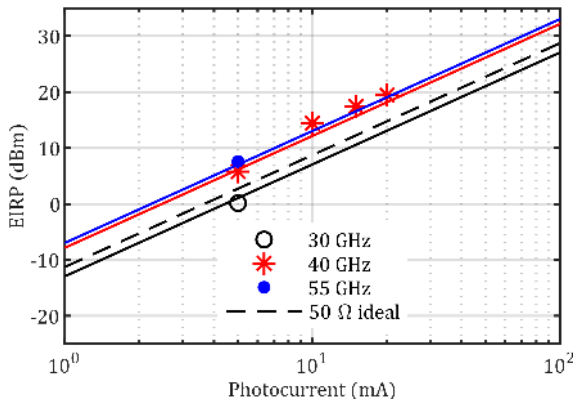


Fig. 15. Measured (markers) and simulated (lines) EIRP values for the fabricated array as a function of the dc photocurrent per channel.

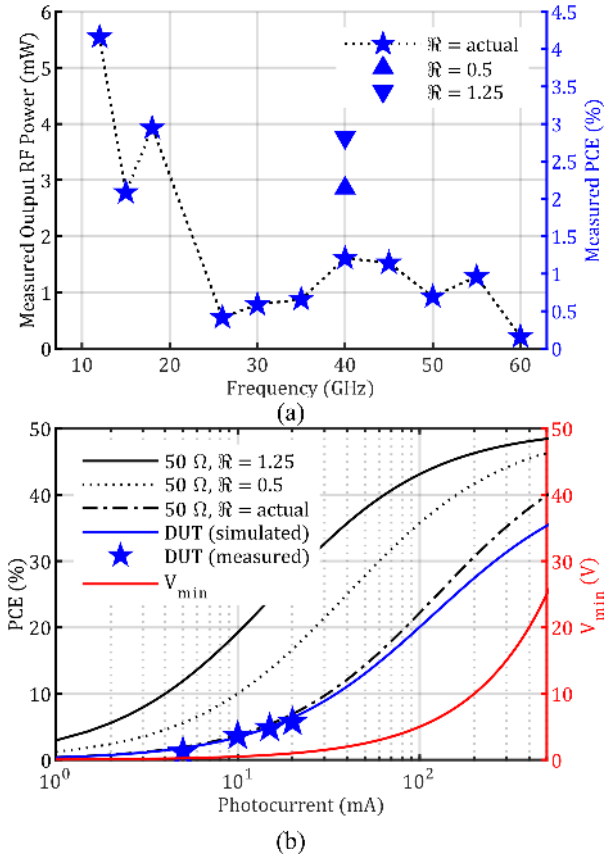


Fig. 16. PCE for the fabricated array. (a) Measured (pentagrams) and simulated (triangles) values as a function of frequency. (b) Measured (pentagrams) and simulated (lines) values as a function of the dc photocurrent per channel at 40 GHz.

at 40 GHz (Fig. 13) imply that increased gain may have also led to increased measured EIRP values.

A maximum EIRP of 19.4 dBm was measured at midband with 20 mA dc photocurrent per channel. During testing at 25 mA per channel, one of the photodiodes exhibited thermal failure, thereby inhibiting further testing of the array. Thermal failure at 25 mA is considered premature for CC-MUTC photodiodes operating at these frequencies [39] and is suspected as being hastened by potential fabrication stressors such as bond degradation due to substrate flexure or suboptimal junction illumination due to the optical components shifting during their UV cure cycle. With improved integration techniques and each photodiode operating near saturation (≈55 mA) [39], EIRP is expected to reach values upward of 30 dBm.

Whereas the EIRP describes the ability of the antenna to generate power and radiate that power in a direction of maximum radiation, i.e., to radiate directionally, the photodiode PCE describes the ability of the antenna to convert its input power to output power. Accordingly, efficiency was evaluated using

$$PCE = \sum_{n=1}^{3} \alpha_n \left[ \frac{P_{out}}{P_{in}^{elec} + P_{in}^{opt}} \right]_n = \sum_{n=1}^{3} \alpha_n \left[ \frac{\alpha_n P_{out}}{I_{dc} V_b + \frac{I_{dc}}{\Re_n}} \right] \tag{30}$$

where $P_{in}^{elec}$ is the input electrical power, i.e., the power dissipated in the photodiode junction, $P_{in}^{opt}$ is the input optical power, and $\alpha_n$ is a weighting factor determined by the responsivity of each channel, i.e., $\alpha_n = \Re_n/(\Re_1 + \Re_2 + \Re_3)$. Using the measured power, as shown in Fig. 13(a), 5 mA dc photocurrent per channel, an applied bias of 3 V per channel, and the measured responsivities given in Table III, the PCE for the fabricated array is shown in Fig. 16(a). In addition to the PCE for each measured frequency, also shown is the expected PCE at 40 GHz given the theoretical maximum responsivity for the photodiodes used in this work under surface-normal illumination at a wavelength of 1550 nm (0.50 A/W) and the theoretical maximum responsivity for an illumination wavelength of 1550 nm (1.25 A/W). As shown, the measured PCE at midband is 1.2% and the maximum value, given 0.50 A/W responsivity, is 2.1% at 5 mA dc photocurrent. As expected, the measured PCE is approximately half the maximum PCE due to the photodiodes being aligned at half responsivity. Much like EIRP, the PCE is expected to increase significantly with increasing photocurrent. In order to determine the PCE dependence on photocurrent, the applied bias voltage, $V_b$, from (30) was replaced with the minimum applied bias voltage, $V_{min}$, from (18) and $P_{out}$ was expanded to give

$$PCE = \sum_{n=1}^{3} \alpha_n \left[ \frac{\frac{1}{2}|i_a|^2 \left(R_{in}^{p}\right)_n}{I_{dc} V_{min} + \frac{I_{dc}}{\Re_n}} \right] \tag{31}$$

where $(R_{in}^{p})_{n=1,2,3}$ is the simulated input resistance for each channel. Fig. 16(b) shows the measured and simulated PCE as a function of the dc photocurrent at 40 GHz for the fabricated array. The measured values were calculated using (30), the measured output RF powers described for EIRP and Fig. 15, and the measured responsivity values from Table III. The simulated values were calculated using (31), simulated $(R_{in}^{p})_{n=1,2,3}$, and measured responsivity values from Table III. In addition, comparisons to a perfectly matched load and with higher responsivities are also shown. As shown, the fabricated array is near its 50 Ω ideal and is expected to reach a PCE of 15% with each photodiode operating near saturation (≈55 mA, 3 V) [39]. This 15% maximum PCE for the fabricated array is assuming the responsivity values of 0.12, 0.17,

and 0.18 A/W that resulted from an intentional defocusing of the optical beam in an attempt to illuminate the photodiode junction uniformly, as discussed in Section III-C. For future implementations, illumination using a collimated beam should be considered, as it is expected to allow the photodiodes to operate at maximum responsivity without sacrificing saturation performance [65], e.g., a responsivity of 0.50 A/W with a collimated beam would result in a maximum PCE of 30% for the fabricated array. To further increase the PCE, the saturation point of the detectors could be pushed to higher photocurrent via improved thermal management [42], e.g., using diamond as the antenna substrate [48], or manipulation of the optical input can be used, e.g., modulation depth enhancement [48].

## V. Conclusion

The design, fabrication, and characterization of an RF photonic TCA for UWB transmit operation at mmW frequencies has been presented. Driven by integrated photodiodes, the array capitalizes on the low-loss and scalable integration potential realized by an optical feed network. A prototype array with $1 \times 3$ active channels has been fabricated and characterized. The array exhibits a maximum EIRP of 19.4 dBm at 40 GHz and a 3 dB (VSWR $< 1.4$) radiated power bandwidth of 1.8:1 across 30–55 GHz. To the best of our knowledge, this is the highest reported bandwidth for a fabricated phased array operating at these frequencies [23], [49]–[51].

Although the fabricated array demonstrates efficient mmW transmission, future work must focus on fabrication strategies to optimize integration density and extend functionality to two dimensions. The 2-D array implementation will see improvements to bandwidth as higher channel counts lead to a closer approximation of a CSA as well as inherent improvements in directivity and EIRP, all of which are critical for high-frequency wireless links.

## Acknowledgment

The authors would like to thank Dr. J. Campbell and Dr. A. Beling of the University of Virginia, Charlottesville, VA, USA, for permission to use their CC-MUTC photodiode design, as well as Dr. G. Pomrenke of AFOSR and Dr. R. Nelson of AFRL for their support of this work.

## References

[1] G. C. Tavik *et al.*, "The advanced multifunction RF concept," *IEEE Trans. Microw. Theory Techn.*, vol. 53, no. 3, pp. 1009–1020, Mar. 2005, doi: 10.1109/TMTT.2005.843485.

[2] C. Hemmi, R. T. Dover, F. German, and A. Vespa, "Multifunction wide-band array design," *IEEE Trans. Antennas Propag.*, vol. 47, no. 3, pp. 425–431, Mar. 1999, doi: 10.1109/8.768776.

[3] S. Rangan, T. S. Rappaport, and E. Erkip, "Millimeter-wave cellular wireless networks: Potentials and challenges," *Proc. IEEE*, vol. 102, no. 3, pp. 366–385, Mar. 2014, doi: 10.1109/JPROC.2014.2299397.

[4] H. T. Friis, "A note on a simple transmission formula," *Proc. IRE*, vol. 34, no. 5, pp. 254–256, May 1946, doi: 10.1109/JRPROC.1946.234568.

[5] M. Marcus and B. Pattan, "Millimeter wave propagation: Spectrum management implications," *IEEE Microw. Mag.*, vol. 6, no. 2, pp. 54–62, Jun. 2005, doi: 10.1109/MMW.2005.1491267.

[6] D. W. Prather *et al.*, "Optically upconverted, spatially coherent phased-array-antenna feed networks for beam-space MIMO in 5G cellular communications," *IEEE Trans. Antennas Propag.*, vol. 65, no. 12, pp. 6432–6443, Dec. 2017, doi: 10.1109/TAP.2017.2735549.

[7] Federal Communications Commission. (Sep. 15, 2016). *The FCC's 5G FAST Plan*. Accessed: Feb. 15, 2019. [Online]. Available: https://www.fcc.gov/5G

[8] C. A. Balanis, "Antenna theory: A review," *Proc. IEEE*, vol. 80, no. 1, pp. 7–23, Jan. 1992, doi: 10.1109/5.119564.

[9] I. Tzanidis, K. Sertel, and J. L. Volakis, "Interwoven spiral array (ISPA) with a 10:1 bandwidth on a ground plane," *IEEE Antennas Wireless Propag. Lett.*, vol. 10, pp. 115–118, 2011, doi: 10.1109/LAWP.2010.2070786.

[10] R. W. Kindt and W. R. Pickles, "All-metal flared-notch array radiator for ultrawideband applications," Defense Tech. Inf. Center, Fort Belvoir, VA, USA, Tech. Rep., Sep. 2010, doi: 10.21236/ADA530583.

[11] W. F. Moulder, K. Sertel, and J. L. Volakis, "Superstrate-enhanced ultrawideband tightly coupled array with resistive FSS," *IEEE Trans. Antennas Propag.*, vol. 60, no. 9, pp. 4166–4172, Sep. 2012, doi: 10.1109/TAP.2012.2210292.

[12] B. A. Munk, *Finite Antenna Arrays and FSS*. Hoboken, NJ, USA: Wiley, 2003.

[13] H. A. Wheeler, "The radiation resistance of an antenna in an infinite array or waveguide," *Proc. IRE*, vol. 36, no. 4, pp. 478–487, Apr. 1948, doi: 10.1109/JRPROC.1948.229650.

[14] H. Wheeler, "Simple relations derived fom a phased-array antenna made of an infinite current sheet," *IEEE Trans. Antennas Propag.*, vol. 13, no. 4, pp. 506–514, Jul. 1965, doi: 10.1109/TAP.1965.1138456.

[15] R. C. Hansen, "Dipole array scan performance over a wide-band," *IEEE Trans. Antennas Propag.*, vol. 47, no. 5, pp. 956–957, May 1999, doi: 10.1109/8.774162.

[16] R. C. Hansen, *Phased Array Antennas*. Hoboken, NJ, USA: Wiley, 1998.

[17] A. Neto and J. J. Lee, "'Infinite bandwidth' long slot array antenna," *IEEE Antennas Wireless Propag. Lett.*, vol. 4, pp. 75–78, 2005, doi: 10.1109/LAWP.2005.844141.

[18] D. Cavallo, A. Neto, and G. Gerini, "Analysis of common-mode resonances in arrays of connected dipoles and possible solutions," in *Proc. Eur. Radar Conf. (EuRAD)*, Sep. 2009, pp. 441–444.

[19] M. Jones and J. Rawnick, "A new approach to broadband array design using tightly coupled elements," in *Proc. IEEE Mil. Commun. Conf. (MILCOM)*, Oct. 2007, pp. 1–7, doi: 10.1109/MILCOM.2007.4454764.

[20] S. S. Holland and M. N. Vouvakis, "The banyan tree antenna array," *IEEE Trans. Antennas Propag.*, vol. 59, no. 11, pp. 4060–4070, Nov. 2011, doi: 10.1109/TAP.2011.2164177.

[21] S. S. Holland and M. N. Vouvakis, "The planar ultrawideband modular antenna (PUMA) array," *IEEE Trans. Antennas Propag.*, vol. 60, no. 1, pp. 130–140, Jan. 2012, doi: 10.1109/TAP.2011.2167916.

[22] S. S. Holland, D. H. Schaubert, and M. N. Vouvakis, "A 7–21 GHz dual-polarized planar ultrawideband modular antenna (PUMA) array," *IEEE Trans. Antennas Propag.*, vol. 60, no. 10, pp. 4589–4600, Oct. 2012, doi: 10.1109/TAP.2012.2207321.

[23] M. H. Novak, F. A. Miranda, and J. L. Volakis, "Ultra-wideband phased array for millimeter-wave ISM and 5G bands, realized in PCB," *IEEE Trans. Antennas Propag.*, vol. 66, no. 12, pp. 6930–6938, Dec. 2018, doi: 10.1109/TAP.2018.2872177.

[24] J. A. Kasemodel, C.-C. Chen, and J. L. Volakis, "Wideband planar array with integrated feed and matching network for wide-angle scanning," *IEEE Trans. Antennas Propag.*, vol. 61, no. 9, pp. 4528–4537, Sep. 2013, doi: 10.1109/TAP.2013.2266090.

[25] J. P. Doane, K. Sertel, and J. L. Volakis, "A wideband, wide scanning tightly coupled dipole array with integrated balun (TCDA-IB)," *IEEE Trans. Antennas Propag.*, vol. 61, no. 9, pp. 4538–4548, Sep. 2013, doi: 10.1109/TAP.2013.2267199.

[26] W. F. Moulder, K. Sertel, and J. L. Volakis, "Ultrawideband superstrate-enhanced substrate-loaded array with integrated feed," *IEEE Trans. Antennas Propag.*, vol. 61, no. 11, pp. 5802–5807, Nov. 2013, doi: 10.1109/TAP.2013.2280001.

[27] A. K. Awasthi and A. R. Harish, "Wideband tightly-coupled compact array of dipole antennas arranged in triangular lattice," *Int. J. Microw. Wireless Technol.*, vol. 11, no. 4, pp. 382–389, Dec. 2018, doi: 10.1017/S1759078718001605.

[28] J. J. Lee *et al.*, "Photonic wideband array antennas," *IEEE Trans. Antennas Propag.*, vol. 43, no. 9, pp. 966–982, Sep. 1995, doi: 10.1109/8.410214.

[29] G. J. Schneider, J. A. Murakowski, C. A. Schuetz, S. Shi, and D. W. Prather, "Radiofrequency signal-generation system with over seven octaves of continuous tuning," *Nature Photon.*, vol. 7, no. 2, pp. 118–122, Feb. 2013, doi: 10.1038/nphoton.2012.339.

[30] J. Bai *et al.*, "Optically driven ultrawideband phased array with an optical interleaving feed network," *IEEE Antennas Wireless Propag. Lett.*, vol. 13, pp. 47–50, 2014, doi: 10.1109/LAWP.2013.2295917.
[31] S. Shi *et al.*, "Conformal wideband optically addressed transmitting phased array with photonic receiver," *J. Lightw. Technol.*, vol. 32, no. 20, pp. 3468–3477, Oct. 15, 2014, doi: 10.1109/JLT.2014.2317191.
[32] T. P. McKenna, J. A. Nanzer, and T. R. Clark, "Photonic beamsteering of a millimeter-wave array with 10-Gb/s data transmission," *IEEE Photon. Technol. Lett.*, vol. 26, no. 14, pp. 1407–1410, Jul. 2014, doi: 10.1109/LPT.2014.2326332.
[33] *Single Mode Fibers*. Accessed: Dec. 11, 2019. [Online]. Available: https://shop.ozoptics.com/sm-fibers
[34] *GORE Microwave/RF Assemblies, 7 Series for Military Aircraft*. Accessed: Dec. 11, 2019. [Online]. Available: https://www.gore.com/products/gore-r-microwave-sealed-airframe-assemblies-7-series
[35] M. R. Konkol *et al.*, "High-power photodiode-integrated-connected array antenna," *J. Lightw. Technol.*, vol. 35, no. 10, pp. 2010–2016, May 15, 2017, doi: 10.1109/JLT.2017.2662604.
[36] D. D. Ross *et al.*, "Low-profile high-power optically addressed phased array antenna," *J. Lightw. Technol.*, vol. 35, no. 18, pp. 3894–3900, Sep. 15, 2017, doi: 10.1109/JLT.2017.2726458.
[37] M. R. Konkol *et al.*, "Photonic tightly coupled array," *IEEE Trans. Microw. Theory Techn.*, vol. 66, no. 5, pp. 2570–2578, May 2018, doi: 10.1109/TMTT.2017.2787552.
[38] E. A. Alwan, K. Sertel, and J. L. Volakis, "Circuit model based optimization of ultra-wideband arrays," in *Proc. IEEE Int. Symp. Antennas Propag.*, Jul. 2012, pp. 1–2, doi: 10.1109/APS.2012.6348919.
[39] Q. Zhou, A. S. Cross, A. Beling, Y. Fu, Z. Lu, and J. C. Campbell, "High-power V-band InGaAs/InP photodiodes," *IEEE Photon. Technol. Lett.*, vol. 25, no. 10, pp. 907–909, May 2013, doi: 10.1109/LPT.2013.2253766.
[40] C. A. Balanis, *Antenna Theory: Analysis and Design*. Hoboken, NJ, USA: Wiley, 2012.
[41] S. M. Sze and K. K. Ng, *Physics of Semiconductor Devices*. Hoboken, NJ, USA: Wiley, 2006.
[42] K. J. Williams and R. D. Esman, "Design considerations for high-current photodetectors," *J. Lightw. Technol.*, vol. 17, no. 8, pp. 1443–1454, 1999, doi: 10.1109/50.779167.
[43] V. J. Urick, K. J. Williams, and J. D. McKinney, *Fundamentals of Microwave Photonics*. Hoboken, NJ, USA: Wiley, 2015.
[44] D. A. Tulchinsky, J. B. Boos, D. Park, P. G. Goetz, W. S. Rabinovich, and K. J. Williams, "High-current photodetectors as efficient, linear, and high-power RF output stages," *J. Lightw. Technol.*, vol. 26, no. 4, pp. 408–416, 2008, doi: 10.1109/JLT.2007.912503.
[45] D. A. Tulchinsky, X. Li, N. Li, S. Demiguel, J. C. Campbell, and K. J. Williams, "High-saturation current wide-bandwidth photodetectors," *IEEE J. Sel. Topics Quantum Electron.*, vol. 10, no. 4, pp. 702–708, Jul. 2004, doi: 10.1109/JSTQE.2004.831951.
[46] N. Li *et al.*, "High-saturation-current charge-compensated InGaAs–InP Uni-traveling-carrier photodiode," *IEEE Photon. Technol. Lett.*, vol. 16, no. 3, pp. 864–866, Mar. 2004, doi: 10.1109/LPT.2004.823773.
[47] X. Li *et al.*, "High-saturation-current InP-InGaAs photodiode with partially depleted absorber," *IEEE Photon. Technol. Lett.*, vol. 15, no. 9, pp. 1276–1278, Sep. 2003, doi: 10.1109/LPT.2003.816118.
[48] X. Xie *et al.*, "Improved power conversion efficiency in high-performance photodiodes by flip-chip bonding on diamond," *Optica*, vol. 1, no. 6, p. 429, Dec. 2014, doi: 10.1364/OPTICA.1.000429.
[49] B. J. DeLong, S. Reddy Govindarajulu, M. H. Novak, E. A. Alwan, and J. L. Volakis, "A 60 GHz phased array with measurement and de-embedding techniques," *Anal. Integr. Circuits Signal Process.*, vol. 97, no. 3, pp. 557–563, Dec. 2018, doi: 10.1007/s10470-018-1295-1.
[50] S. M. Moghaddam, J. Yang, and A. A. Glazunov, "A planar dual-polarized ultra-wideband millimeter-wave array antenna," in *Proc. 12th Eur. Conf. Antennas Propag. (EuCAP)*, 2018, pp. 1–3, doi: 10.1049/cp.2018.0360.
[51] S. M. Moghaddam, J. Yang, and A. U. Zaman, "Fully-planar ultrawideband tightly-coupled array (FPU-TCA) with integrated feed for wide-scanning millimeter-wave applications," *IEEE Trans. Antennas Propag.*, vol. 68, no. 9, pp. 6591–6601, Sep. 2020, doi: 10.1109/TAP.2020.3001448.
[52] D. D. Ross, "RF photonic apertures," M.S. thesis, Dept. Elect. Comput. Eng., Univ. Delaware, Newark, DE, USA, 2018.
[53] A. J. Mercante, D. L. K. Eng, M. Konkol, P. Yao, S. Shi, and D. W. Prather, "Thin $LiNbO_3$ on insulator electro-optic modulator," *Opt. Lett.*, vol. 41, no. 5, p. 867, Mar. 2016, doi: 10.1364/OL.41.000867.
[54] T.-C. Tzu, K. Sun, R. Costanzo, D. Ayoub, S. M. Bowers, and A. Beling, "Foundry-enabled high-power photodetectors for microwave photonics," *IEEE J. Sel. Topics Quantum Electron.*, vol. 25, no. 5, pp. 1–11, Sep. 2019, doi: 10.1109/JSTQE.2019.2911458.
[55] Y. Wang *et al.*, "High-power photodiodes with 65 GHz bandwidth heterogeneously integrated onto Silicon-on-Insulator nano-waveguides," *IEEE J. Sel. Topics Quantum Electron.*, vol. 24, no. 2, pp. 1–6, Mar. 2018, doi: 10.1109/JSTQE.2017.2712625.
[56] Q. Li *et al.*, "High-power evanescently coupled waveguide MUTC photodiode with >105-GHz bandwidth," *J. Lightw. Technol.*, vol. 35, no. 21, pp. 4752–4757, Nov. 1, 2017, doi: 10.1109/JLT.2017.2759210.
[57] Z. Li, H. Pan, H. Chen, A. Beling, and J. C. Campbell, "High-saturation-current modified uni-traveling-carrier photodiode with cliff layer," *IEEE J. Quantum Electron.*, vol. 46, no. 5, pp. 626–632, May 2010, doi: 10.1109/JQE.2010.2046140.
[58] N. Li *et al.*, "High-saturation-current charge-compensated InGaAs–InP uni-traveling-carrier photodiode," *IEEE Photon. Technol. Lett.*, vol. 16, no. 3, pp. 864–866, Mar. 2004, doi: 10.1109/LPT.2004.823773.
[59] N. Shimizu, N. Watanabe, T. Furuta, and T. Ishibashi, "InP-InGaAs uni-traveling-carrier photodiode with improved 3-dB bandwidth of over 150 GHz," *IEEE Photon. Technol. Lett.*, vol. 10, no. 3, pp. 412–414, Mar. 1998, doi: 10.1109/68.661427.
[60] T. Ishibashi, S. Kodama, N. Shimizu, and T. Furuta, "High-speed response of uni-traveling-carrier photodiodes," *Jpn. J. Appl. Phys.*, vol. 36, no. Part 1, No. 10, pp. 6263–6268, Oct. 1997, doi: 10.1143/JJAP.36.6263.
[61] J. Huang, "The finite ground plane effect on the microstrip antenna radiation patterns," *IEEE Trans. Antennas Propag.*, vol. 31, no. 4, pp. 649–653, Jul. 1983, doi: 10.1109/TAP.1983.1143108.
[62] R. Marg, I. Schon, and A. F. Jacob, "Finite ground plane effects on the radiation pattern of small microstrip arrays," *IEE Proc.-Microw., Antennas Propag.*, vol. 147, no. 2, pp. 139–143, Apr. 2000, doi: 10.1049/ip-map:20000095.
[63] T. Namiki, Y. Murayama, and K. Ito, "Improving radiation-pattern distortion of a patch antenna having a finite ground plane," *IEEE Trans. Antennas Propag.*, vol. 51, no. 3, pp. 478–482, Mar. 2003, doi: 10.1109/TAP.2003.809838.
[64] T. Ishibashi, Y. Muramoto, T. Yoshimatsu, and H. Ito, "Unitraveling-carrier photodiodes for terahertz applications," *IEEE J. Sel. Topics Quantum Electron.*, vol. 20, no. 6, pp. 79–88, Nov. 2014, doi: 10.1109/JSTQE.2014.2336537.
[65] A. Joshi and D. Becker, "GRIN lens-coupled top-illuminated photodetectors for high-power applications," in *Proc. Microw. Photon., Int. Top. Meeting*, Oct. 2007, pp. 18–20, doi: 10.1109/MWP.2007.4378124.

**Victoria A. Carey** received the B.E.E. degree from the University of Delaware, Newark, DE, USA, in 2014, where she is currently pursuing the Ph.D. degree in electrical engineering with a concentration in electromagnetics and photonics, while functioning as an Engineer at Phase Sensitive Innovations, Inc., Newark.

**Matthew R. Konkol** received the B.A. degree in physics and mathematics from SUNY Geneseo, Geneseo, NY, USA, in 2010, and the Ph.D. degree in electrical engineering with a concentration in electromagnetics and photonics from the University of Delaware, Newark, DE, USA, in 2017.

While attending the University of Delaware, he specialized in radio frequency (RF) photonics with an emphasis in phased array antenna design and high-speed electrooptic modulator and photodetector design, fabrication, and characterization. He joined Phase Sensitive Innovations, Inc., Newark, in 2017, as a Lead Engineer in photonic component research and development and is currently working on mmW phased array antenna design and commercialization of high-power photodetectors. His current research interests include broadband phased arrays, high-performance photodetectors, and microwave photonic links.

**Shouyuan Shi** received the B.S., M.S., and Ph.D. degrees in electrical engineering from Xidian University, Xi'an, China, in 1991, 1994, and 1997, respectively.

He is currently a Research Professor with the Department of Electrical and Computer Engineering, the University of Delaware, Newark, DE, USA. He has authored or coauthored 8 books and book chapters and more than 270 peer-refereed journal and conference publications. His research interests include computational electromagnetics, microoptics and nanophotonics, electrooptics and radio frequency (RF) photonics, antennas, microwave and millimeter wave imaging, nanophotonic devices, including metamaterials, plasmonics, photonic bandgap materials, and dispersion engineered photonic crystals, and software development.

Dr. Shi is a Topic Editor of *Photonic Devices and Materials and Optical and Photonic Letters*. He is an Editorial Board Member of *Advances in Optics*. He is also an active reviewer for more than 20 international peer-reviewed journals in the areas of optics and photonics, electrooptics, and electromagnetics.

**Andrew J. Mercante** received the B.E.E. and Ph.D. degrees in electrical engineering with a concentration in electromagnetics and photonics from the University of Delaware, Newark, DE, USA, in 2013 and 2018, respectively.

He is currently a Senior Engineer at Phase Sensitive Innovations, Inc., Newark, leading research and development and commercialization efforts in thin-film lithium niobate modulators. His current research interests include electrooptic devices with terahertz operational bandwidths and heterogeneous integration for millimeter-wave photonic applications.

**Kevin Shreve** received the B.S. degree in industrial technology/nuclear science from the Louisiana State University, Baton Rouge, LA, USA, in 1986.

Since graduating, he has worked for over 30 years as a Research and Development Engineer in optoelectronics, photovoltaics, and radio frequency (RF) photonics for companies, such as AstroPower, Inc., G.E Energy, Blue Square Energy, and Phase Sensitive Innovations, Inc., Newark, where he is currently a Research and Development Engineer focusing on process development, device fabrication, and packaging/integration. He has authored or coauthored over 20 technical papers.

**Andrew A. Wright** received the B.S. degree in electronic engineering and the M.S. degree in electromagnetics and photonics from the University of Delaware, Newark, DE, USA, in 2011 and 2015, respectively. His M.S. thesis was on the research and development of a 95 GHz low-noise amplifier (LNA) using SiGe:BiCMOS technology.

After transitioning to Phase Sensitive Innovations, Inc., Newark, he has continued in the development of integrated circuit design. He has experience in high-frequency characterization that includes S-parameter analyses up to 300 GHz, noise figure measurements, and saturated power analyses. He has extensive experience in packaging efforts, including pick and place, wire bonding, and flip-chip bonding of die-level components. His experience also expands to hardware development that includes creating 3-D models for production of mechanical components, 3-D printing of components, and assembly.

**Christopher A. Schuetz** received the B.S. degree in electrical engineering from Virginia Polytechnic and State University, Blacksburg, VA, USA, in 1997, and the M.S. and Ph.D. degrees in the area of millimeter-wave imaging from the University of Delaware, Newark, DE, USA, in 2004 and 2007, respectively.

Since graduating with honors, he has been with companies, such as BAE Systems and Optical Crosslinks, Inc., where his research interests include microwave photonics and polymer optical waveguides. He is currently a Research Assistant Professor at the University of Delaware and the Chief Technology Officer of Phase Sensitive Innovations, Inc., Newark, where he is investigating the application of optics to millimeter-wave (mmW) detection and imaging. His expertise is in mmW imaging, phenomenology, and detection, where he has authored or coauthored more than 20 technical papers.

Dr. Schuetz has served on the committee for the SPIE Passive Millimeter Wave Imaging Technology Conference, served as a Co-Editor of a special issue of Applied Optics on radio frequency (RF) imaging, and served as the Co-Chair of a SPIE Photonics West Session on RF and mmW Photonics.

**Dennis W. Prather** (Fellow, IEEE) received the B.S.E.E., M.S.E.E., and Ph.D. degrees from the University of Maryland at College Park, College Park, MD, USA, in 1989, 1993, and 1997, respectively.

He is currently the College of Engineering Distinguished Professor with the Department of Electrical and Computer Engineering, University of Delaware, Newark, DE, USA. The focus of this laboratory is on both the theoretical and experimental aspects of active and passive nanophotonic elements and their integration into optoelectronic subsystems. To achieve this, the laboratory develops and refines computational electromagnetic tools for both the analysis and synthesis of photonic devices in addition to developing nanofabrication and integration processes necessary for their integration into functional subsystems.